COLD-FORMED HIGH STRENGTH STEEL CHS-to-RHS T- AND X-JOINTS: PERFORMANCE AND DESIGN AFTER FIRE EXPOSURES

Madhup Pandey[1,*] and Ben Young[2]

[1]Department of Civil Engineering, University of Nottingham, Nottingham, United Kingdom.
[2]Department of Civil and Environmental Engineering, The Hong Kong Polytechnic University, Hong Kong, China.

Abstract

The post-fire structural performance of cold-formed high strength steel (CFHSS) T- and X-joints with circular hollow section (CHS) braces and square and rectangular hollow section (SHS and RHS) chords is numerically investigated in this study. The tubular members had the nominal 0.2% proof stress of 900 MPa. The CHS-to-RHS T- and X-joints were subjected to compression loads through brace members. The nominal values of peak fire temperatures (ψ) were 300°C, 550°C, 750°C and 900°C. Tests carried out by the authors investigating the post-fire static response of cold-formed S900 steel grade CHS-to-RHS T- and X-joints were formed the basis of the numerical investigation carried out in this study. The test results reported by the authors were used to develop accurate finite element (FE) models. The validated FE models were used to perform extensive numerical parametric studies comprising 768 FE specimens. The validity ranges of critical geometric parameters were extended beyond current limits mentioned in international codes and guides. The residual strengths of test and FE specimens were compared with the nominal resistances predicted from design equations given in Eurocode 3 and *Comité International pour le Développement et l´Etude de la Construction Tubulaire* (CIDECT) Design Guide 3 using the measured post-fire residual material properties. Generally, design rules given in Eurocode 3 and CIDECT are shown to be quite conservative with very dispersed unreliable predictions. As a result, accurate and reliable design rules are proposed in this study.

Keywords: *Cold-formed Steel; Fire; High Strength Steel; Hollow Section Joint; Post-fire; Tubular Members.*

[*]Corresponding author. (e-mail: madhup.pandey@nottingham.ac.uk).

1. Introduction

Owing to rapid increase in fire incidents of structures in recent years, the post-fire assessments of fire exposed structures are important. Without scientific assessments, structures exposed to high temperatures cannot be allowed for their direct reuse. During the cooling phase, the temperature of steel drops down, and eventually, the steel material would shrink. Consequently, the thermal-induced shrinkage deformations would lock inside the fire exposed structural steel members, and the situation could be dangerous. Thus, a reliable evaluation method is required to confirm whether a fire exposed structure should be allowed for its direct reuse, repair or just demolish, thereby highlighting the strategic importance of the post-fire assessment [1]. The outcomes of the post-fire investigation facilitate various stakeholders of the property to opt for best reuse strategies for fire exposed structures. Generally, steel structures are more vulnerable to fires compared to concrete structures, which in turn highlight the critical importance of post-fire investigation of fire exposed steel structures. In addition to various structural applications, it is worth noting that CHS-to-RHS joints have also been used in the manufacture of equipment and structural systems in the road transport and agricultural industries [2]. Moreover, Fig. 1 presents a pedestrian truss bridge with CHS brace and RHS chord at Westminster Millennium Pier in London, United Kingdom [3].

Tubular members are frequently used in both onshore and offshore structures subjected to different types of loading because of high torsional strength, ability to confine in-filled material, superior aesthetic appearance and so on. Tubular member made of high strength steel (HSS) (in this paper, HSS refers to steels with steel grades higher than S460) provides additional merits, including superior strength per unit weight, reduced handling costs and time. Primarily, the focus of investigations on tubular joints in the last six decades was on their structural performance at room temperature, while investigations of tubular joints at peak fire temperatures (ψ) largely remain exiguous. The post-fire behaviour of circular hollow section (CHS) T-joints made of Q345B steel grade was investigated by Jin et al. [4]. It was concluded that the effect of preload on the residual capacities of fire exposed CHS T-joints was negligible. Experimental and numerical studies were carried out by Gao et al. [5] to investigate the cyclic performance of fire exposed CHS T-joints made of normal strength steel (in this study, refer to steels with steel grades less than or equal to S460). The CHS T-joints were reinforced with doubler plates. It was noticed that the energy dissipation capacities of CHS T-joints were significantly reduced after fire exposures. The post-fire behaviour of concrete in-filled CHS T-joints was experimentally and numerically investigated by Gao et al. [6]. It was found that the residual capacities of fire exposed concrete in-filled CHS T-joints were less than the corresponding fire exposed hollow CHS T-joints. Pandey and Young [7] carried out tests to investigate the residual strengths ($N_{f,\psi}$) of ISO-834 [8] fire exposed cold-formed S900 steel grade T- and X-joints with CHS braces and square and rectangular hollow section (SHS and RHS) chords. The literature review confirmed that except above mentioned studies, no other investigation is available on the post-fire behaviour of normal and high strength steel tubular joints. It should be noted that, henceforth, RHS also includes SHS in this paper.

A detailed numerical investigation was performed in this study to gain an in-depth understanding of various critical parameters that affected the static behaviour of CHS-to-RHS T- and X-joints. Accurate finite element (FE) models were developed for CHS-to-RHS T- and X-joints using the test results reported in Pandey and Young [7]. The validated FE models were used to perform extensive numerical parametric studies that comprised 768 FE specimens, including 384 T-joints and 384 X-joints made of CHS braces and RHS chords. The residual strengths ($N_{f,\psi}$) of test [7] and FE specimens were compared with the nominal resistances predicted from design equations given in EC3 [9] and CIDECT [10] using the measured post-fire residual material properties investigated by Pandey and Young [1]. Generally, it has been demonstrated that the predictions from design rules given in EC3 [9] and CIDECT [10] are quite conservative but largely dispersed and unreliable for the range of fire exposed CHS-to-RHS T- and X-joints investigated in this study. Therefore, using two design approaches, accurate and reliable design equations are proposed in this study to predict the residual strengths ($N_{f,\psi}$) of cold-formed S900 steel grade CHS-to-RHS T- and X-joints subjected to post-fire temperatures ranging from 300°C to 900°C.

2. Outline of test programs on CHS-to-RHS T- and X-joints under post-fire conditions

The static residual strengths of cold-formed high strength steel (CFHSS) fire exposed CHS-to-RHS T- and X-joints subjected to compression loads were investigated by Pandey and Young [7]. Before conducting the static joint tests, the test specimens were subjected to a total of three fire exposures. The preselected peak temperatures (ψ) of three fire exposures were 300°C, 550°C and 750°C, respectively. In total, 7 T-joints and 7 X-joints made of CHS braces and RHS chords were fabricated. The nominal 0.2% proof stress of hollow section members was 900 MPa. The braces and chords were welded using robotic metal active gas welding. The test specimens were grouped in 3 series for the 3 fire exposures (i.e. ψ_1=300°C, ψ_2=550°C and ψ_3=750°C). All 3 series of CHS-to-RHS T- and X-joints test specimens were exposed to fire inside a gas furnace, where the furnace temperature was increased in accordance with ISO-834 [8]. After attaining the preselected peak temperatures (ψ), the test specimens were allowed to naturally cool inside the furnace. Subsequently, CHS-to-RHS T- and X-joints test specimens were tested at room temperature by applying compression loads through brace members. Fig. 2 presents the definitions of various notations for CHS-to-RHS X-joints, which remain valid for CHS-to-RHS T-joints. The static behaviour of CHS-to-RHS T- and X-joints primarily depends on geometric ratios, namely β (d_1/b_0), τ (t_1/t_0) and 2γ (b_0/t_0). The symbols b, h, t and R stand for cross-section width, depth, thickness and external corner radius of tubular member, respectively. The symbol d denotes the diameter of CHS member. The subscripts 0 and 1 represent chord and brace, respectively. In the experimental investigation, β varied from 0.74 to 0.89, τ varied from 0.76 to 1.02 and 2γ varied from 25.1 to 30.6.

The lengths of braces (L_1) were equal to two times the brace diameter (d_1). On the other hand, the lengths of chords (L_0) were equal to $h_1 + 3h_0 + 180$ and $h_1 + 3h_0$ for T- and X-joints, respectively. The test results were obtained in the form of $N_{f,\psi}$ vs u and $N_{f,\psi}$ vs v curves, where $N_{f,\psi}$, u and v respectively stand for residual load, chord face indentation and chord side wall deformation. It should be noted that $N_{f,\psi}$ vs u curves were used to determine the $N_{f,\psi}$ of fire exposed CHS-to-RHS T- and X-joints. The material properties of ISO-834 [8] fire exposed cold-formed S900 steel grade CHS and

RHS members were investigated by Pandey and Young [1] for post-fire temperatures ranging from 300°C to 900°C. The test specimens in the experimental program [7] were fabricated from tubular members that belonged to the identical batch of tubes used in Pandey and Young [1]. Thus, the material properties of fire exposed CHS and RHS members can be referred to Pandey and Young [1]. It should be noted that the cold-formed S900 steel grade CHS-to-RHS T- and X-joints [7] and tubular members [1] were simultaneously exposed to fire inside the gas furnace. The measured values of static yield strength of fire exposed tubular members ranged from 1033 to 1087 MPa for ψ_1=300°C, 889 to 991 MPa for ψ_2=550°C, 269 to 371 MPa for ψ_3=750°C and 233 to 390 MPa for ψ_4=900°C.

3. Numerical program

3.1. Finite element (FE) models of CHS-to-RHS T- and X-joints

3.1.1. General

ABAQUS [11] was used to perform comprehensive FE analyses in this study. As the induced strains in the FE models during the applied load were unidirectional, the isotropic strain hardening law was selected for the analysis. The yielding onsets of FE models in this study were based on the von-Mises yield theory. The default Newton-Raphson method was used to find the roots of non-linear equilibrium equations. The material non-linearities were considered in the FE models by assigning the measured values of post-fire residual static stress-strain curves of flat, corner and curved portions of RHS and CHS members in the plastic material definition part of the FE models. However, experimentally obtained constitutive material curves were transformed into true stress-strain curves prior to their inclusion in the FE models. On the other hand, the geometric non-linearities in FE models were considered by enabling the non-linear geometry parameter (*NLGEOM) in ABAQUS [11], which allowed the FE models to undergo large displacement during the analyses. Furthermore, various parameters, including through-thickness division, contact interactions, mesh seed spacing, corner region extension and element types, were also studied and reported in the following sections of this paper. The labelling of parametric FE specimens was kept identical to the label system used in the test program [7]. Figs. 3 and 4 present typical CHS-to-RHS T- and X-joints FE specimens modelled in this study, respectively.

3.1.2. Element type, material properties and mesh spacing

Except for the welds, all other parts of the FE models were developed using second-order hexahedral elements, particularly using the C3D20 elements. On the other hand, the second-order tetrahedral element, C3D10, was used to model the weld parts owing to their complicated shapes. The use of solid elements helped in making realistic fusions between tubular and weld parts of the FE models. Convergence studies were conducted using different mesh sizes, and finally, chord and brace members were seeded at 4 mm and 7 mm intervals, respectively, along their corresponding longitudinal and transverse directions. Moreover, the seeding spacings of weld parts reciprocated the seeding spacings of their respective brace parts. In order to ensure the smooth transfer of stresses from flange to web regions, the corner portions of RHS were split into ten elements. FE analyses were also conducted to examine the influence of divisions along the wall thickness (t) of tubular members. The results of these FE analyses demonstrated the trivial influence of wall thickness divisions on the load vs deformation curves of the investigated CHS-to-RHS T- and X-joints. The use of the C3D20 element as well as the small thickness of test specimens [7] led to such observations. It is worth noting that similar findings were also noticed by Pandey et al. [12,13] and Pandey and Young [14,15]. Thus, for the validations of FE models, the wall thicknesses of tubular members were not divided.

The measured post-fire static stress-strain curves of flat and corner portions of RHS members and curved portion of CHS members were used in the FE models. In this study, the influence of cold-working in RHS members was included by assigning wider corner portions in the FE models. Various distances for corner extension were considered in the sensitivity analyses, and finally, the corner portions of RHS members were extended by $2t$ into the neighbouring flat portions, which agreed with other studies [12-21] conducted on CFHSS tubular members and joints.

3.1.3. Weld modelling and contact interactions

The fillet welds were modelled in all FE specimens using the average values of measured weld sizes reported in Pandey and Young [7]. The inclusions of weld geometries improved the overall accuracies of FE models. In addition, modelling of weld parts helped in attaining realistic load transfer between brace and chord members. The selection of the C3D10 element maintained optimum stiffness around the joint perimeter due to its ability to take complicated shapes. In total, two types of contact interactions were defined in CHS-to-RHS T- and X-joints FE models. First, contact interaction between brace and chord members of CHS-to-RHS T- and X-joints FE models. Second, contact interaction between chord members and chord end bearing blocks of CHS-to-RHS T-joint FE models. Both contact interactions were established using the built-in surface-to-surface contact definition. In addition, a tie constraint was also established between weld and tubular members of CHS-to-RHS T- and X-joints FE models. The contact interactions between brace and chord members of CHS-to-RHS T- and X-joints FE models was kept frictionless, while a frictional penalty equal to 0.3 was imposed on the contact interaction between chord member and chord end bearing blocks of CHS-to-RHS T-joint FE models. Along the normal direction of these two contact interactions, a 'hard' contact pressure overclosure was used. In addition, finite sliding was permitted between the interaction surfaces. For contact interactions and tie constraint, the surfaces were connected to each other using the 'master-slave' algorithm technique.

3.1.4. Boundary conditions

The boundary conditions in CHS-to-RHS T- and X-joints FE models were assigned by creating reference points. Three reference points were created for the CHS-to-RHS T-joint FE model, including one top reference point (TRP) and two bottom reference points (BRP-1 and BRP-2), as shown in Fig. 3. The TRP replicated the fixed boundary condition of the top brace end, while BRP-1 and BRP-2 replicated the boundary conditions of roller positioned at each chord end. The TRP was created at the cross-section centre of the top brace end, while BRP-1 and BRP-2 were created at 20 mm below the centre of the bottom surfaces of chord end bearing blocks. The TRP, BRP-1 and BRP-2 were then coupled to their corresponding surfaces using the built-in kinematic coupling type. In order to exactly replicate the boundary conditions of the CHS-to-RHS T-joint test setup, all degrees of freedom (DOF) of TRP were restrained. On the other hand, for BRP-1 and BRP-2, except for the translations along the vertical and longitudinal directions of the CHS-to-RHS T-joint FE specimen as well as the rotation about the transverse direction of the chord member, all other DOF of BRP-1 and BRP-2 were also restrained. In addition, all DOF of other nodes of CHS-to-RHS T-joint FE specimen were kept unrestrained for both rotation and translation.

With regard to the CHS-to-RHS X-joint FE model, the top and bottom reference points (TRP and BRP) were created at the cross-section centres of the top and bottom brace members, as shown in Fig. 4. Subsequently, TRP and BRP were coupled to their respective brace end cross-section surfaces using the kinematic coupling type. In order to exactly replicate the boundary conditions of the CHS-to-RHS X-joint test setup, all DOF of TRP were restrained. However, except for the vertical translation, all other DOF of BRP were also restrained. Moreover, all DOF of other nodes of the CHS-to-RHS X-joint FE specimen were kept unrestrained for both rotation and translation. Using the displacement control method, compression load was then applied at the bottom reference points of the CHS-to-RHS T- and X-joints FE models. In addition, the size of the step increment was kept small in order to obtain smooth load vs deformation curves. Following this approach, the boundary conditions and load applications in FE models were identical to the test program [7].

3.2. Validations of CHS-to-RHS T- and X-joints FE models

The numerical modelling techniques described in the preceding section of this paper were used to develop CHS-to-RHS T- and X-joints FE models. The validations were performed by comparing the residual strengths ($N_{f,\psi}$), load vs deformation histories and failure modes of test and FE specimens. The measured dimensions of tubular members and welds were used to develop all FE models. In addition, measured post-fire residual static material properties of tubular members were used in the validation process. It is worth mentioning that both ultimate load and 3% deformation limit (i.e. $0.03b_0$) load were used to determine the $N_{f,\psi}$ of test and FE specimens, whichever occurred earlier in the $N_{f,\psi}$ vs u curves. The residual strengths ($N_{f,\psi}$) of CHS-to-RHS T- and X-joints test specimens were compared with those predicted from their corresponding FE models (N_{FE}), as shown in Tables 1 and 2, respectively. Referring to Table 1, the mean (P_m) and coefficients of variation (COV) (V_p) of the comparisons for CHS-to-RHS T-joints are 1.02 and 0.009, respectively. On the other hand, as shown in Table 2, the P_m and V_p of the comparisons for CHS-to-RHS X-joints are 0.99 and 0.007, respectively. In addition, the comparisons of load vs deformation curves between CHS-to-RHS T- and X-joints test and FE specimens are shown in Figs. 5 and 6, respectively. Moreover, Figs. 7 and 8 present the comparisons of failure modes between typical CHS-to-RHS T- and X-joints test and FE specimens, respectively. From Tables 1-2 and Figs. 5-8, it can therefore be concluded that the validated FE models precisely replicated the overall static behaviour of CFHSS fire exposed CHS-to-RHS T- and X-joints.

3.3. Parametric study of CHS-to-RHS T- and X-joints

3.3.1. General

In the parametric study, 4 fire exposures with peak temperatures (ψ) equal to 300°C, 550°C, 750°C and 900°C were investigated, which were consistent with the test programs [1,7]. In total, 768 FE analyses were performed in the parametric study, including 384 CHS-to-RHS T-joints and 384 CHS-to-RHS X-joints. The validity ranges of important geometric ratios were purposefully widened beyond the present limitations set by EC3 [9] and CIDECT [10]. Table 3 presents the overall ranges of various critical parameters considered in the numerical investigation. In the parametric study, all FE modelling techniques described earlier in this paper were used.

3.3.2. Details of finite element models

The values of brace diameter of parametric FE specimens varied from 15 mm to 450 mm, while the values of cross-section width and depth of RHS chords of parametric FE specimens varied from 50 mm to 500 mm. However, the values of wall thickness of braces and chords varied from 2 mm to 10 mm. The external corner radius of RHS member (R_0) conformed to commercially produced HSS members [22]. In this study, R_0 was kept as $2t$ for $t \leq 6$ mm, $2.5t$ for $6 < t \leq 10$ mm and $3t$ for $t > 10$ mm, which in turn also meet the limits detailed in EN 10219-2 [23]. The formulae used to determine the lengths of braces and chords of CHS-to-RHS T- and X-joints FE specimens were identical to those used in the test program [7]. For meshing along the longitudinal and transverse directions of

RHS members, seedings were approximately spaced at the minimum of $b/30$ and $h/30$. On the other hand, CHS brace members were meshed approximately at an interval of $d/30$. Overall, the adopted mesh sizes of parametric FE specimens varied from 3 mm to 12 mm. On the other hand, the seeding interval of weld parts of parametric FE specimens reciprocated the seeding interval of their corresponding brace parts.

For precise replication of RHS curvatures, the corner portions of RHS members were split into ten parts. Likewise, in the validation process, the corner portions of RHS members were extended by $2t$ into their neighbouring flat portions. For tubular members with $t \leq 6$ mm, no divisions were made along the wall thickness of the parametric FE specimens. However, when $t > 6$ mm, the wall thickness of parametric FE specimens was divided into two layers. Following the prequalified tubular joint details given in AWS D1.1M [24], the leg size (w) of the fillet weld of CHS-to-RHS T- and X-joints FE specimens was designed as 1.5 times the minimum of t_1 and t_0, which was consistent with the test program [7]. For different fire exposure series (i.e. ψ_1=300°C, ψ_2=550°C, ψ_3=750°C and ψ_4=900°C) of the FE parametric study, the corresponding measured post-fire residual static material properties of CHS 88.9×4 and RHS 120×60×4 [1] were respectfully assigned to the CHS and RHS members of the FE specimens. Figs. 9 and 10 present the measured post-fire residual static stress-strain curves of CHS 88.9×4 and RHS 120×60×4 for different fire exposure series, respectively. Besides, the measured static weld material properties at room temperature [25] were retained as 100%, 85%, 57% and 48% for 300°C, 550°C, 750°C and 900°C post-fire temperatures, respectively. These retention percentages correspond to the average retention values of the ultimate stress of tubular members of different fire exposure series. Table 4 presents the measured post-fire residual static material properties of CHS 88.9×4 and RHS 120×60×4 adopted in the parametric study, which include Young's modulus (E), 0.2% proof stress and strain ($\sigma_{0.2}$ and $\varepsilon_{0.2}$), ultimate stress and strain (σ_u and ε_u) and fracture strain (ε_f).

3.3.3. Failure modes of CHS-to-RHS T- and X-joints under post-fire conditions

Overall, two types of failure modes were identified for both CHS-to-RHS T- and X-joints. First, the failure of CHS-to-RHS T- and X-joints by the yielding of chord flange, which was named as chord face failure and denoted by the letter 'F' in this study. Second, the failure of CHS-to-RHS T- and X-joints due to the combination of chord face and chord side wall failure modes, which was named as the combined failure mode and denoted by 'F+S' in this study. It is important to note that these failure modes were defined corresponding to the $N_{f,\psi}$, which in turn was computed by combinedly considering the ultimate and $0.03b_0$ limit loads, whichever occurred earlier in the $N_{f,\psi}$ vs u curve. The test and parametric FE specimens were failed by the F mode, when the $N_{f,\psi}$ was determined using the $0.03b_0$ limit. The applied loads of fire exposed CHS-to-RHS T- and X-joints failed by the F mode were monotonically increasing. The CHS-to-RHS T- and X-joints were failed by the F mode in this investigation, when $0.30 \leq \beta < 0.75$. For test and parametric FE specimens that failed by the F+S mode, the load vs deformation curves exhibited clear ultimate load. Additionally, evident deformations of chord flange, chord webs and chord corner regions were noticed in the test and parametric FE specimens that failed by the F+S mode. The CHS-to-RHS T- and X-joints were failed by the F+S mode in this investigation, when $0.75 \leq \beta \leq 0.90$. Moreover, none of the test and FE specimens were failed by the global buckling of braces. Figs. 11 and 12 present the variations of $N_{f,\psi}$ vs u curves of typical CHS-to-RHS T- and X-joints FE specimens that failed by the F and F+S modes for different post-fire temperatures investigated in this study, respectively.

4. EC3 (2005) and CIDECT (2009) design provisions

Currently, design rules to predict the post-fire residual strengths of tubular joints are not given in any code and guideline. Therefore, in order to examine the suitability of EC3 [9] and CIDECT [10] design provisions for CFHSS fire exposed CHS-to-RHS T- and X-joints, in this study, the nominal resistances from design equations given in EC3 [9] and CIDECT [10] ($N_{E,\psi}$ and $N_{C,\psi}$) were determined using the measured post-fire residual static material properties shown in Table 4. The design rules given in EC3 [9] and CIDECT [10] are shown below:

Chord face failure ($\beta \leq 0.85$)

EC3 [9]:

$$N_{E,\psi} = C_f \left[\frac{\pi}{4} k_n \frac{f_{y0,\psi} t_0^2}{(1-\beta)\sin\theta_1} \left(\frac{2\eta}{\sin\theta_1} + 4\sqrt{1-\beta} \right) / \gamma_{M5} \right] \tag{1}$$

CIDECT [10]:

$$N_{C,\psi} = C_f \left[\frac{\pi}{4} Q_f \frac{f_{y0,\psi} t_0^2}{\sin\theta_1} \left(\frac{2\eta}{(1-\beta)\sin\theta_1} + \frac{4}{\sqrt{1-\beta}} \right) \right] \tag{2}$$

Chord side wall failure ($\beta = 1.0$)

EC3 [9]:

$$N_{E,\psi} = C_f \left[\frac{\pi}{4} k_n \frac{f_{b,\psi} t_0}{\sin\theta_1} \left(\frac{2d_1}{\sin\theta_1} + 10t_0 \right) / \gamma_{M5} \right] \tag{3}$$

CIDECT [10]:

$$N_{C,\psi} = C_f \left[\frac{\pi}{4} Q_f \frac{f_{k,\psi} t_0}{\sin\theta_1} \left(\frac{2d_1}{\sin\theta_1} + 10t_0 \right) \right] \tag{4}$$

The nominal resistances of CHS-to-RHS T- and X-joints from design equations given in EC3 [9] were determined using 0.2% proof stress and partial safety factor (γ_{M5}) equal to 1.0. In addition, a material factor (C_f) equal to 0.80 was adopted as per EC3 [26]. On the other hand, CIDECT [10] uses the minimum of 0.2% proof stress and 0.80 times the corresponding ultimate stress for joint resistance calculation. Moreover, design provisions given in CIDECT [10] recommend the use of C_f equal to 0.90 for tubular joints with steel grade exceeding S355. Unlike EC3 [9], CIDECT [10] uses different values of partial safety factors (γ_M) for different types of tubular joints and their corresponding failure modes, which are given in IIW [27]. However, their effects are implicitly included inside the CIDECT [10] design provisions. In this study, nominal resistances of CHS-to-RHS X-joints from design equations given in CIDECT [10] were calculated using γ_M equal to 1.0 and 1.25 for chord face failure and chord side wall failure modes, respectively. On the other hand, nominal resistances of CHS-to-RHS T-joints from design equations given in CIDECT [10] were calculated using γ_M equal to 1.0 for both chord face failure and chord side wall failure modes. In Eqs. (1) to (4), chord stress functions are denoted by k_n and Q_f, post-fire yield stress of chord member is denoted by $f_{y0,\psi}$, the parameter η is equal to d_1/b_0, post-fire chord side wall buckling stresses are denoted by $f_{b,\psi}$ and $f_{k,\psi}$, and the angle between brace and chord is denoted by θ_1 (in degrees). For CHS-to-RHS T-joints, the effect of chord-in-plane bending was considered through k_n and Q_f functions. However, for CHS-to-RHS X-joints, the values of k_n and Q_f were adopted as 1.0.

In addition, a reliability analysis was performed as per AISI S100 [28]. In this study, design equation was treated as reliable when the value of reliability index (β_0) was greater than or equal to 2.50. The values of various statistical parameters and load combinations used in the reliability index calculation are identical to those values adopted in Pandey et al. [12,13] and Pandey and Young [14,15,19-21].

5. Comparisons between residual strengths and nominal resistances

Tables 5 and 6 present the overall summary of comparisons between $N_{f,\psi}$ and nominal resistances predicted from design equations given in EC3 [9] and CIDECT [10] for CHS-to-RHS T-joints failed by the F and F+S failure modes, respectively. On the other hand, Tables 7 and 8 present the overall summary of comparisons between $N_{f,\psi}$ and nominal resistances predicted from design equations given in EC3 [9] and CIDECT [10] for CHS-to-RHS X-joints failed by the F and F+S failure modes, respectively. In total, 782 data are presented in Tables 5 to 8, including 14 test data [7] and 768 parametric FE data generated in this study. The comparisons are also graphically shown in Figs. 13 and 14 for CHS-to-RHS T-joints, and in Figs. 15 and 16 for CHS-to-RHS X-joints.

Table 5 presents the overall summary of comparisons for CHS-to-RHS T-joint test and FE specimens that failed by the F mode. It can be noticed that the design rules given in EC3 [9] are found to be slightly unconservative and unreliable when nominal resistances are predicted using the post-fire material properties. In addition, predictions are largely dispersed. On the contrary, the design rules in CIDECT [10] are found to be slightly conservative but unreliable when the post-fire material properties are used to predict the nominal resistances. Moreover, predictions are also largely dispersed. For CHS-to-RHS T-joint test and FE specimens that failed by the F+S mode, the design rules given in EC3 [9] and CIDECT [10] are found to be quite conservative but unreliable, as shown in Table 6. Furthermore, when using the post-fire material properties, the predictions from design equations given in EC3 [9] and CIDECT [10] are quite dispersed.

With regard to CHS-to-RHS X-joint test and FE specimens that failed by the F mode, the overall summary of comparisons is shown in Table 7. It is evident that, when using post-fire material properties, the design rules given in EC3 [9] and CIDECT [10] are found to be slightly conservative but unreliable. In addition, predictions are largely dispersed. On the other hand, Table 8 presents the overall summary of comparisons for CHS-to-RHS X-joint test and FE specimens that failed by the F+S mode. The design rules given in EC3 [9] and CIDECT [10] are found to be quite conservative but unreliable. Moreover, predictions calculated using post-fire material properties are quite dispersed.

In Figs. 13 and 15, generally, test and parametric FE specimens with small values of β and η ratios and large values of 2γ ratio lie below the unit slope line (i.e. y=x). For such specimens, the joint resistance corresponding to the $0.03b_0$ limit was not sufficient to cause the yielding of chord flanges. On the contrary, the yield line theory was used to derive the existing design equation for RHS T- and X-joints that failed by the F mode. Consequently, the $N_{f,\psi}$ of CHS-to-RHS T- and X-joints specimens became smaller than the corresponding nominal resistances predicted from design equations given in EC3 [9] and CIDECT [10]. As a result, the data of such specimens fall below the line of unit slope. The data above the line of unit slope, on the other hand, indicate CHS-to-RHS T- and X-joints specimens with medium to large values of β and η ratios and small values of 2γ ratio. The stress-strain behaviour of HSS material is quite different to that of mild steel [29-34], which could change the deformation extent of chord connecting face(s). For CHS-to-RHS T- and X-joints that failed by the F+S mode, the data above the unit slope line in Figs. 14 and 16 typically represent specimens with large values of β ratio and small values of 2γ and h_0/t_0 ratios. As the β ratio of CHS-to-RHS T- and X-joints failed by the F+S mode increased, the brace member gradually approached the chord corner regions. Consequently, the $N_{f,\psi}$ of such T- and X-joints increased due to the enhanced rigidity of chord corner regions. On the other hand, the corresponding increase in nominal resistances predicted from design equations given in EC3 [9] and CIDECT [10] was lower than the $N_{f,\psi}$ of CHS-to-RHS T- and X-joints. Subsequently, the data of such specimens fall above the line of unit slope in Figs. 14 and 16.

6. Proposed design rules

Using two design approaches, named as proposal-1 and -2, design rules are proposed in this study for CFHSS fire exposed CHS-to-RHS T- and X-joints failed by F and F+S failure modes. For CFHSS fire exposed CHS-to-RHS T-joints, the design rules proposed in both the approaches (i.e. proposal-1 and -2) are based on the design equations proposed by Pandey et al. [12] for without fire exposed S900 steel grade CHS-to-RHS T-joints. On the other hand, for CFHSS fire exposed CHS-to-RHS X-joints, the proposed design rules under proposal-1 and -2 are based on the design equations proposed by Pandey and Young [15] for S900 steel grade CHS-to-RHS X-joints without fire exposure. In the first design approach (i.e. proposal-1), the room temperature material properties used in the design equations proposed by Pandey et al. [12] and Pandey and Young [15] are replaced with the corresponding post-fire residual material properties. In addition, a correction factor (ξ) based on post-fire peak temperature (ψ) is also applied on the proposed design rules. On the other hand, in the second design approach (i.e. proposal-2), only a correction factor based on the post-fire peak temperature (ψ) is applied on the design rules proposed by Pandey et al. [12] and Pandey and Young [15] using the room temperature material properties. Therefore, design equations under proposal-1 can predict the $N_{f,\psi}$ of fire exposed CHS-to-RHS T- and X-joints when post-fire residual material properties are available. However, design equations under proposal-2 can predict the $N_{f,\psi}$ only using the post-fire peak temperature (ψ).

It should be noted that the design rules proposed in this study are valid for 300°C ≤ ψ ≤ 900°C. In this investigation, the validity ranges of important factors influencing the static behaviour of CHS-to-RHS T- and X-joints were extended beyond their existing limits given in EC3 [9] and CIDECT [10]. Furthermore, as welds were modelled in all parametric FE specimens, the influence of weld was implicitly included in the proposed design rules. In order to obtain design resistances (N_d), the proposed nominal resistances (N_{pn1} and N_{pn2}) shall be multiplied by their correspondingly recommended resistance factors (ϕ), i.e. $N_d = \phi$ (N_{pn1} or N_{pn2}).

6.1. For CHS-to-RHS T-joints

6.1.1. Chord face failure (F) mode ($0.30 \leq \beta < 0.75$)

<u>Proposal-1:</u>

Using post-fire material properties and post-fire peak temperature (ψ) correction factor:

$$N_{pn1} = \xi\left[f_{y0,\psi} t_0^2 \left(\frac{1.2e^{3.1\beta}}{0.6 + 0.025(2\gamma)} \right) \right] \quad (5)$$

where

$$\xi = \begin{bmatrix} 0.965 & \text{for} & 300°\text{C} \le \psi \le 550°\text{C} \\ 0.0023\psi - 0.3 & \text{for} & 550°\text{C} < \psi \le 900°\text{C} \end{bmatrix} \quad (6)$$

<u>Proposal-2:</u>

Using room temperature material properties and post-fire peak temperature (ψ) correction factor:

$$N_{pn2} = (1.3 - 0.001\psi)\left[f_{y0} t_0^2 \left(\frac{1.2e^{3.1\beta}}{0.6 + 0.025(2\gamma)} \right) \right] \quad (7)$$

The Eqs. (5) and (7) are valid for $0.30 \le \beta < 0.75$, $16.6 \le 2\gamma \le 50$, $15 \le h_0/t_0 \le 50$ and $0.50 \le \tau \le 0.90$. As shown in Table 5, the P_m and V_p of proposal-1 (i.e. Eq. (5)) are 1.00 and 0.119, respectively, while the P_m and V_p of proposal-2 (i.e. Eq. (7)) are 1.01 and 0.138, respectively. For both Eqs. (5) and (7), ϕ equal to 0.80 is recommended, resulting in β_0 equal to 2.63 and 2.59, respectively. The comparisons of $N_{f,\psi}$ of CHS-to-RHS T-joint specimens with nominal resistances predicted from design equations given in EC3 [9] and CIDECT [10] as well as predictions from proposal-1 and -2 are graphically presented in Fig. 13. In addition, the distributions of the ratios of $N_{f,\psi}$ of CHS-to-RHS T-joint specimens-to-nominal resistances predicted from Eqs. (1), (2), (5) and (7) are shown in Fig. 17.

6.1.2. Combined failure (F+S) mode ($0.75 \le \beta \le 0.90$)

<u>Proposal-1:</u>

Using post-fire material properties and post-fire peak temperature (ψ) correction factor:

$$N_{pn1} = \xi\left[f_{y0,\psi} t_0^2 \left(\frac{57\beta - 30}{0.8 + 0.013(2\gamma)} \right) \right] \quad (8)$$

where

$$\xi = \begin{bmatrix} 0.85 & \text{for} & 300°\text{C} \le \psi \le 550°\text{C} \\ 0.001\psi + 0.3 & \text{for} & 550°\text{C} < \psi \le 900°\text{C} \end{bmatrix} \quad (9)$$

<u>Proposal-2:</u>

Using room temperature material properties and post-fire peak temperature (ψ) correction factor:

$$N_{pn2} = (1.17 - 0.001\psi)\left[f_{y0} t_0^2 \left(\frac{57\beta - 30}{0.8 + 0.013(2\gamma)} \right) \right] \quad (10)$$

The Eqs. (8) and (10) are valid for $0.75 \le \beta \le 0.90$, $16.6 \le 2\gamma \le 50$, $15 \le h_0/t_0 \le 50$ and $0.75 \le \tau$

≤ 1.0. As shown in Table 6, the P_m and V_p of proposal-1 (i.e. Eq. (8)) are 1.03 and 0.124, respectively, while the P_m and V_p of proposal-2 (i.e. Eq. (10)) are 1.05 and 0.145, respectively. For Eqs. (8) and (10), ϕ equal to 0.85 and 0.80 are recommended which resulted in β_0 equal to 2.50 and 2.69, respectively. The comparisons of $N_{f,\psi}$ of CHS-to-RHS T-joint specimens with nominal resistances predicted from design equations given in EC3 [9] and CIDECT [10] as well as predictions from proposal-1 and -2 are graphically presented in Fig. 14. In addition, the distributions of the ratios of $N_{f,\psi}$ of CHS-to-RHS T-joint specimens-to-nominal resistances predicted from Eqs. (1) to (4), (8) and (10) are shown in Fig. 18.

6.2. For CHS-to-RHS X-joints

6.2.1. Chord face failure (F) mode ($0.30 \leq \beta < 0.75$)

<u>Proposal-1:</u>

Using post-fire material properties and post-fire peak temperature (ψ) correction factor:

$$N_{pn1} = \xi\left[f_{y0,\psi} t_0^2 \left(\frac{1.5e^{3\beta}}{0.65 + 0.025(2\gamma)} \right) \right] \tag{11}$$

where

$$\xi = \begin{bmatrix} 0.915 & \text{for} \quad 300°\text{C} \leq \psi \leq 550°\text{C} \\ 0.0023\psi - 0.35 & \text{for} \quad 550°\text{C} < \psi \leq 900°\text{C} \end{bmatrix} \tag{12}$$

<u>Proposal-2:</u>

Using room temperature material properties and post-fire peak temperature (ψ) correction factor:

$$N_{pn2} = (1.28 - 0.001\psi)\left[f_{y0} t_0^2 \left(\frac{1.5e^{3\beta}}{0.65 + 0.025(2\gamma)} \right) \right] \tag{13}$$

The Eqs. (11) and (13) are valid for $0.30 \leq \beta < 0.75$, $16.6 \leq 2\gamma \leq 50$, $15 \leq h_0/t_0 \leq 50$ and $0.50 \leq \tau \leq 0.90$. As shown in Table 7, the P_m and V_p of proposal-1 (i.e. Eq. (11)) are 1.01 and 0.139, respectively, while the P_m and V_p of proposal-2 (i.e. Eq. (13)) are 1.01 and 0.148, respectively. For both Eqs. (11) and (13), ϕ equal to 0.80 is recommended, resulting in β_0 equal to 2.58 and 2.55, respectively. The comparisons of $N_{f,\psi}$ of CHS-to-RHS X-joint specimens with nominal resistances predicted from design equations given in EC3 [9] and CIDECT [10] as well as predictions from proposal-1 and -2 are graphically presented in Fig. 15. In addition, the distributions of the ratios of $N_{f,\psi}$ of CHS-to-RHS X-joint specimens-to-nominal resistances predicted from Eqs. (1), (2), (11) and

(13) are shown in Fig. 19.

6.2.2. Combined failure (F+S) mode ($0.75 \leq \beta \leq 0.90$)

<u>Proposal-1:</u>

Using post-fire material properties and post-fire peak temperature (ψ) correction factor:

$$N_{pn1} = \xi \left[f_{y0,\psi} t_0^2 \left(\frac{65\beta - 35}{0.75 + 0.015(2\gamma)} \right) \right] \quad (14)$$

where

$$\xi = \begin{bmatrix} 0.9 & \text{for} \quad 300°\text{C} \leq \psi \leq 550°\text{C} \\ 0.001\psi + 0.35 & \text{for} \quad 550°\text{C} < \psi \leq 900°\text{C} \end{bmatrix} \quad (15)$$

<u>Proposal-2:</u>

Using room temperature material properties and post-fire peak temperature (ψ) correction factor:

$$N_{pn2} = (1.17 - 0.001\psi) \left[f_{y0} t_0^2 \left(\frac{65\beta - 35}{0.75 + 0.015(2\gamma)} \right) \right] \quad (16)$$

The Eqs. (14) and (16) are valid for $0.75 \leq \beta \leq 0.90$, $16.6 \leq 2\gamma \leq 50$, $15 \leq h_0/t_0 \leq 50$ and $0.75 \leq \tau \leq 1.0$. As shown in Table 8, the P_m and V_p of proposal-1 (i.e. Eq. (14)) are 1.00 and 0.107, respectively, while the P_m and V_p of proposal-2 (i.e. Eq. (16)) are 1.08 and 0.131, respectively. For Eqs. (14) and (16), ϕ equal to 0.80 and 0.85 are recommended which resulted in β_0 equal to 2.68 and 2.63, respectively. The comparisons of $N_{f,\psi}$ of CHS-to-RHS X-joint specimens with nominal resistances predicted from design equations given in EC3 [9] and CIDECT [10] as well as predictions from proposal-1 and -2 are graphically presented in Fig. 16. In addition, the distributions of the ratios of $N_{f,\psi}$ of CHS-to-RHS X-joint specimens-to-nominal resistances predicted from Eqs. (1) to (4), (14) and (16) are shown in Fig. 20.

7. Conclusions

This paper presents post-fire static behaviour and design of cold-formed S900 steel grade T- and X-joints made of circular hollow section (CHS) braces and square and rectangular hollow section (SHS and RHS) chords. In this study, CHS-to-RHS T- and X-joints specimens were numerically investigated under compression loads. Test results of cold-formed S900 steel grade CHS-to-RHS T-and X-joints reported in Pandey and Young [7] were used to develop accurate finite element (FE) models in this study. The numerical investigation corresponding to 300°C, 550°C, 750°C and 900°C post-fire temperatures was performed using the measured post-fire residual static material properties of S900 steel grade CHS and RHS members investigated by Pandey and Young [1]. A comprehensive numerical parametric study comprising of 768 CHS-to-RHS T- and X-joints specimens was performed using the validated FE models. The inclusion of welds in all FE models appreciably improved the accuracies of the numerical results.

Overall, CHS-to-RHS T- and X-joints specimens were failed by chord face failure (F) mode and a combination of chord face failure and chord side wall failure modes, i.e. combined failure (F+S) mode. The residual static strengths of CHS-to-RHS T- and X-joints specimens corresponding to 300°C, 550°C, 750°C and 900°C post-fire temperatures were compared with the nominal resistances predicted from design equations given in EC3 [9] and CIDECT [10] using the post-fire residual material properties. Generally, it is shown that the design rules in EC3 [9] and CIDECT [10] are unsuitable and unreliable for the range of fire exposed CHS-to-RHS T- and X-joints investigated in this study with extended validity limits of critical geometric parameters. Therefore, using the two design approaches, accurate, less dispersed and reliable design rules are proposed in this study for the design of S900 steel grade CHS-to-RHS T- and X-joints subjected to post-fire temperatures ranging from 300°C to 900°C.

Acknowledgement

The work described in this paper was fully supported by a grant from the Research Grants Council of the Hong Kong Special Administrative Region, China (Project No. 17210218).

References

[1] Pandey M and Young B. Post-fire Mechanical Response of High Strength Steels. Thin-Walled Structures, 164 (2021) 107606.

[2] Mashiri F.R. and Zhao X.L. Plastic mechanism analysis of welded thin-walled T-joints made up of circular braces and square chords under in-plane bending. Thin-Walled Structures, 2004, 42(5), 759-783.

[3] https://www.google.com/maps/place/Westminster+Millennium+Pier/@51.5015009,-0.1235908,3a,75y,90t/data=!3m8!1e2!3m6!1sAF1QipP2Ypm5zAN0SQqlwMT5dc9LnvyI3gTOlgm_grfP!2e10!3e12!6shttps:%2F%2Flh5.googleusercontent.com%2Fp%2FAF1QipP2Ypm5zAN0SQqlwMT5dc9LnvyI3gTOlgm_grfP%3Dw203-h135-k-no!7i4896!8i3264!4m11!1m2!2m1!1sWestminster+Pier+3d!3m7!1s0x487604c42e7e340b:0xa0c700f87873079e!8m2!3d51.5015009!4d-0.1235908!10e5!15sChNXZXN0bWluc3RlciBQaWVyIDNkWhUiE3dlc3RtaW5zdGVyIHBpZXIgM2SSARJ0b3VyaXN0X2F0dHJhY3Rpb27gAQA!16zL20vMDIxcmt4

[4] Jin M, Zhao J, Chang J and Zhang D. Experimental and parametric study on the post-fire behavior of tubular T-joint. Journal of Constructional Steel Research, 70, 93-100. 2012.

[5] Gao F, Gua, XQ, Zhu HP and Xia Y. Hysteretic behaviour of tubular T-joints reinforced with doubler plates after fire exposure. Thin-Walled Structures, 92, 10-20, 2015.

[6] Gao F, Zhu H, Liang H and Tian Y. Post-fire residual strength of steel tubular T-joint with concrete-filled chord. Journal of Constructional Steel Research, 139, 327-338, 2017.

[7] Pandey M and Young B. Post-Fire Behaviour of Cold-Formed High Strength Steel Tubular T- and X-Joints, Journal of Constructional Steel Research 2021;186:106859.

[8] ISO-834. Fire-resistance tests-Elements of Building Construction-Part 1-General requirements. ISO 834-1, International Organization of Standards, 1999.

[9] Eurocode 3 (EC3), Design of Steel Structures-Part 1-8: Design of Joints, EN 1993-1-8, European Committee for Standardization, CEN, Brussels, Belgium, 2005.

[10] Packer JA, Wardenier J, Zhao XL, Vegte GJ van der, Kurobane Y. Design guide for rectangular hollow section (RHS) joints under predominantly static loading. Comite´ International pour le Developpement et l'Etude de la Construction TuECbulaire (CIDECT), Design Guide No. 3, 2nd edn., LSS Verlag, Dortmund, Germany, 2009.

[11] Abaqus/Standard. Version 6.17. USA: K. a. S. Hibbit; 2017.

[12] Pandey M, Chung KF and Young B. Design of cold-formed high strength steel tubular T-joints under compression loads. Thin-Walled Structures 2021;164:107573.

[13] Pandey M, Chung KF and Young B. Numerical investigation and design of fully chord supported tubular T-joints. Engineering Structures 2021;239:112063.

[14] Pandey M and Young B. Static Performance and Design of Cold-formed High Strength Steel Rectangular Hollow Section X-Joints, Engineering Structures, 2023. (in press).

[15] Pandey M and Young B. New Design Rules of Cold-formed High Strength Steel CHS-to-RHS X-Joints, Thin-walled Structures, Elsevier (in press).

[16] Li QY and Young B. Design of cold-formed steel built-up open section members under combined compression and bending. Thin-Walled Structures. 2022;172:108890.

[17] Ma JL, Chan TM and Young B. Design of cold-formed high strength steel tubular beams. Engineering Structures 2017; 151:432-443.

[18] Li HT and Young B. Cold-formed stainless steel RHS members undergoing combined bending and web crippling: Testing, modelling and design. Engineering Structures 2022;250:113466.

[19] Pandey M and Young B. Modelling and Design of Cold-formed S960 Steel Brace-rotated Tubular T- and X-Joints, Journal of Constructional Steel Research, 2023. (in press).

[20] Pandey M and Young B. S960 Steel Grade Square Bird-Beak T- and X-Joints: Numerical Investigation and Design, Journal of Constructional Steel Research, 2023. (in press).
[21] Pandey M and Young B. Design of Cold-formed High Strength Steel Diamond Bird-beak Tubular T- and X-Joints, Journal of Structural Engineering, ASCE, 2023. (in press).
[22] SSAB. Strenx Tube 900 MH. Data Sheet 2042, Sweden, 2017.
[23] prEN 10219-2. Cold formed welded structural hollow sections of non-alloy and fine grain steels-Part 2: Tolerances, dimensions and sectional properties. European Committee for Standardization (CEN), Brussels, Belgium; 2019.
[24] AWS D1.1/D1.1M, Structural Welding Code – Steel, American Welding Society (AWS), Miami, USA, 2020.
[25] Pandey M and Young B. Compression capacities of cold-formed high strength steel tubular T-joints. J Constr Steel Res 2019;162:105650.
[26] Eurocode 3 (EC3), Design of steel structures. Part 1-12: Additional rules for the extension of EN 1993 up to steel grades S700, EN 1993-1-12, European Committee for Standardization, CEN, Brussels, Belgium, 2007.
[27] IIW Doc. XV-1402-12 and IIW Doc. XV-E-12-433. Static design procedure for welded hollow section joints – Recommendations. International Institute of Welding, Paris, France, 2012.
[28] AISI S100. North American Specification for the design of cold-formed steel structural members. American Iron and Steel Institute (AISI), Washington, D.C., USA, 2016.
[29] Pandey M and Young B. Static resistances of cold-formed high strength steel tubular non-90° X-Joints, Engineering Structures 2021;239:112064.
[30] Pandey M and Young B. Ultimate Resistances of Member-Rotated Cold-Formed High Strength Steel Tubular T-Joints under Compression Loads, Engineering Structures 2021;244:112601.
[31] Pandey, M. and Young, B. Stress Concentration Factors of Cold-Formed High Strength Steel Tubular T-Joints. Thin-walled Structures, 2021, 166, 107996.
[32] Pandey, M. and Young, B. Experimental Investigation on Stress Concentration Factors of Cold-formed High Strength Steel Tubular X-Joints. Engineering Structures, 2021, 243, 112408.
[33] Pandey M, Young B. High strength steel tubular X-joints – An experimental insight under axial compression. In: Tubular Structures XVI: Proceedings of Tubular Structures XVI, Melbourne, Australia, pp. 223-230, 2017.
[34] Pandey, M. and Young, B. Effect of Member Orientation on the Static Strengths of Cold-Formed High Strength Steel Tubular X-Joints. Thin-walled Structures, 2022, 170, 108501.

Fig. 1. Pedestrian truss bridge with CHS brace and RHS chord at Westminster Millennium Pier in London [3].

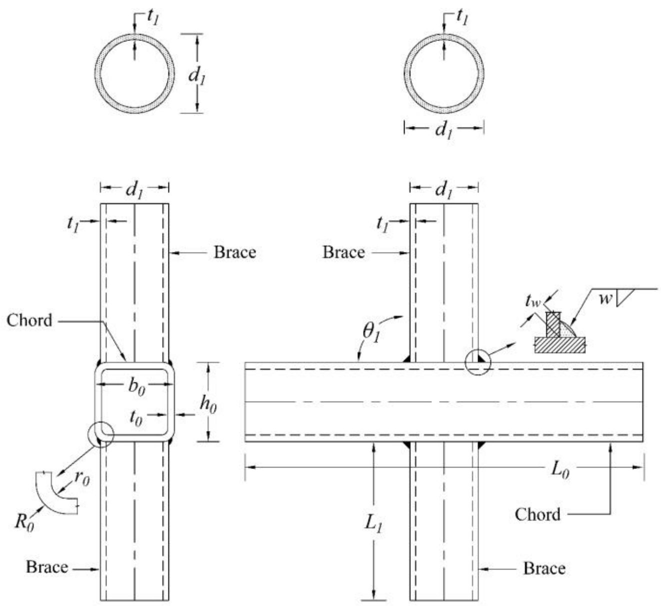

Fig. 2. Definitions of notations for CHS-to-RHS X-joint (also valid for CHS-to-RHS T-joint).

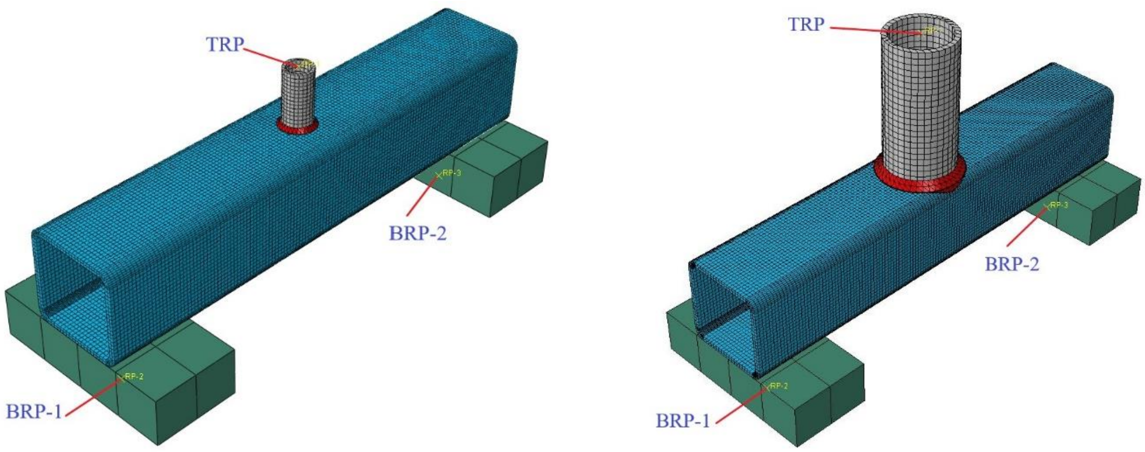

(a) CHS-to-RHS T-joint with β=0.30. (b) CHS-to-RHS T-joint with β=0.80.

Fig. 3. Typical CHS-to-RHS T-joint FE models.

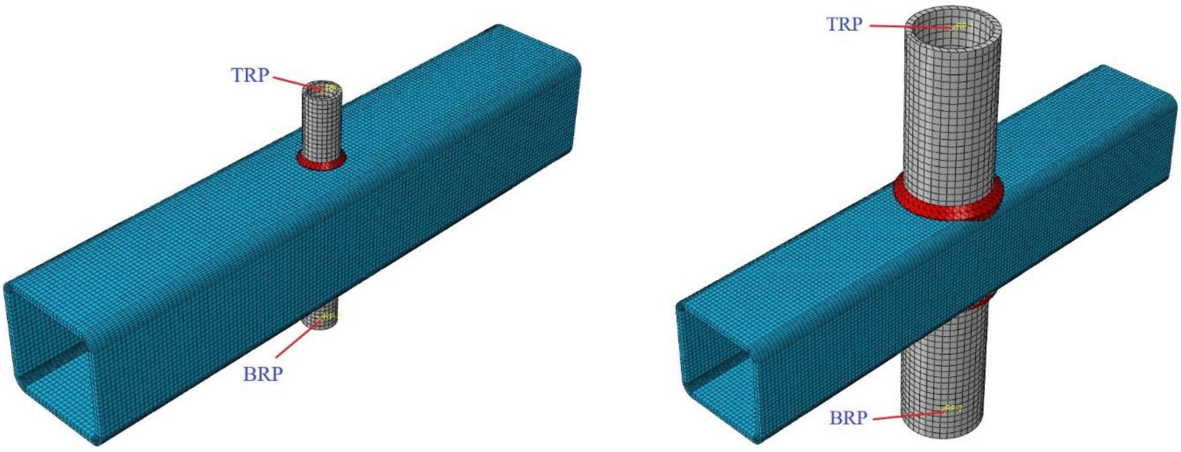

(a) CHS-to-RHS X-joint with β=0.30. (b) CHS-to-RHS X-joint with β=0.80.

Fig. 4. Typical CHS-to-RHS X-joint FE models.

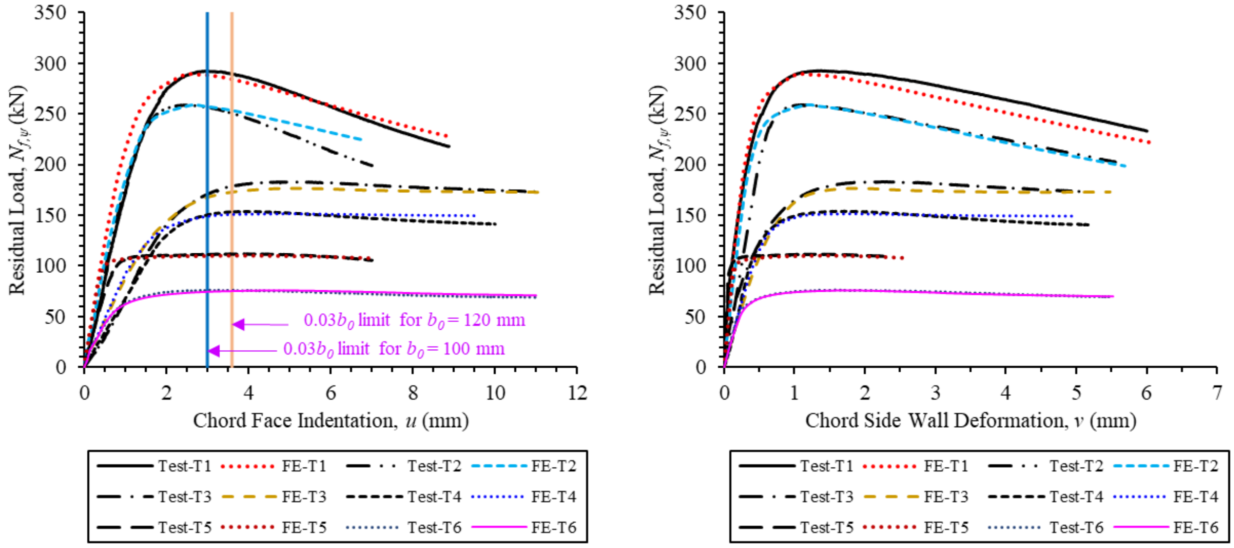

(a) Residual Load vs chord face indentation curves. (b) Residual Load vs chord side wall deformation curves.

Fig. 5. Test vs FE load-deformation curves for CHS-to-RHS T-joints.

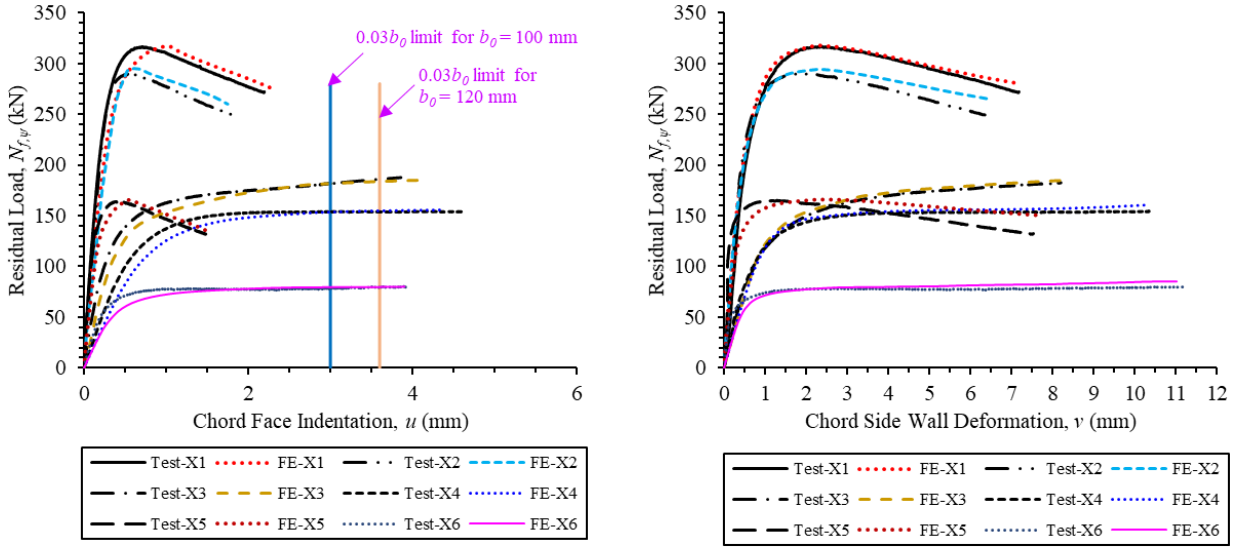

(a) Residual Load vs chord face indentation curves. (b) Residual Load vs chord side wall deformation curves.

Fig. 6. Test vs FE load-deformation curves for CHS-to-RHS X-joints.

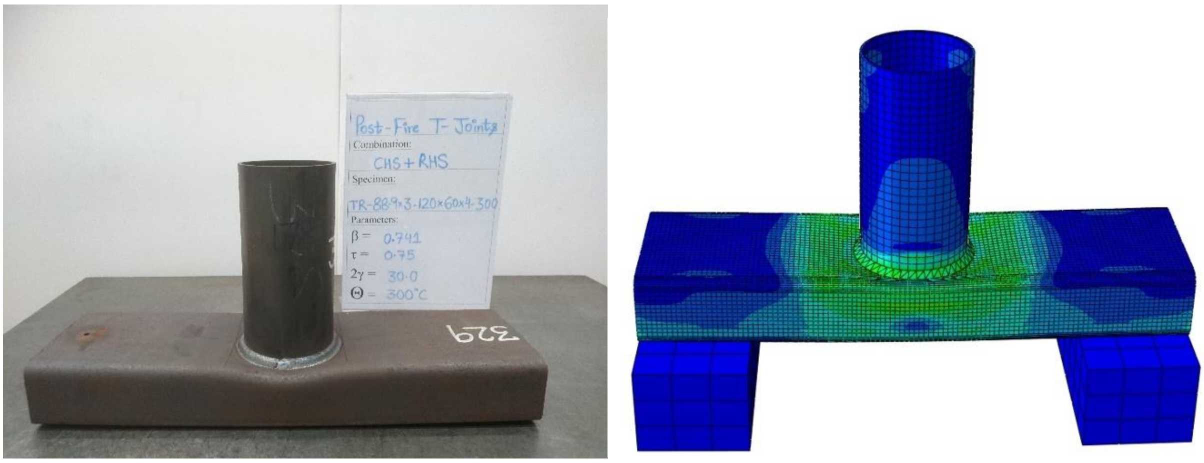

(a) Comparison of test and FE CHS-to-RHS T-joint failed by F mode.

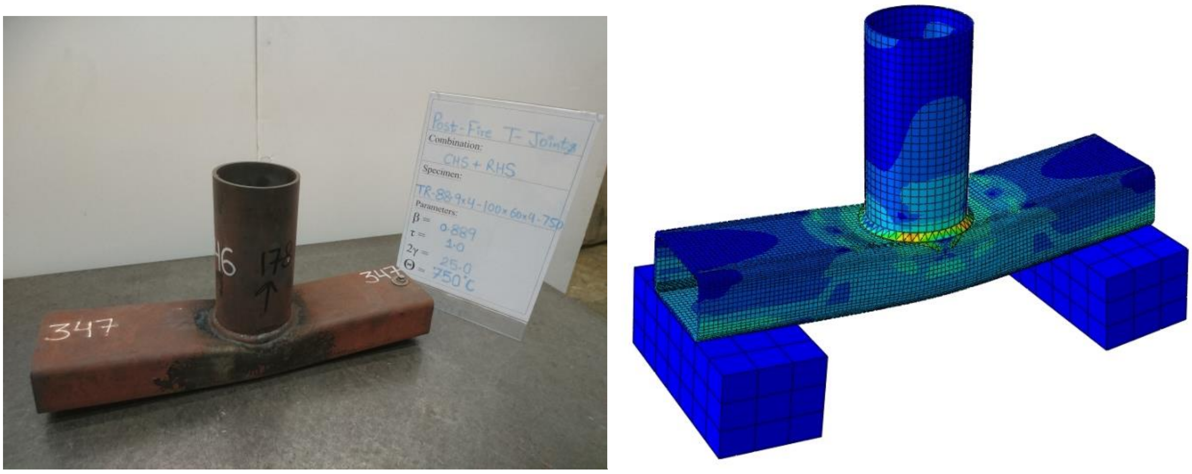

(b) Comparison of test and FE CHS-to-RHS T-joint failed by F+S mode.

Fig. 7. Failure modes comparisons between typical test and FE CHS-to-RHS T-joints.

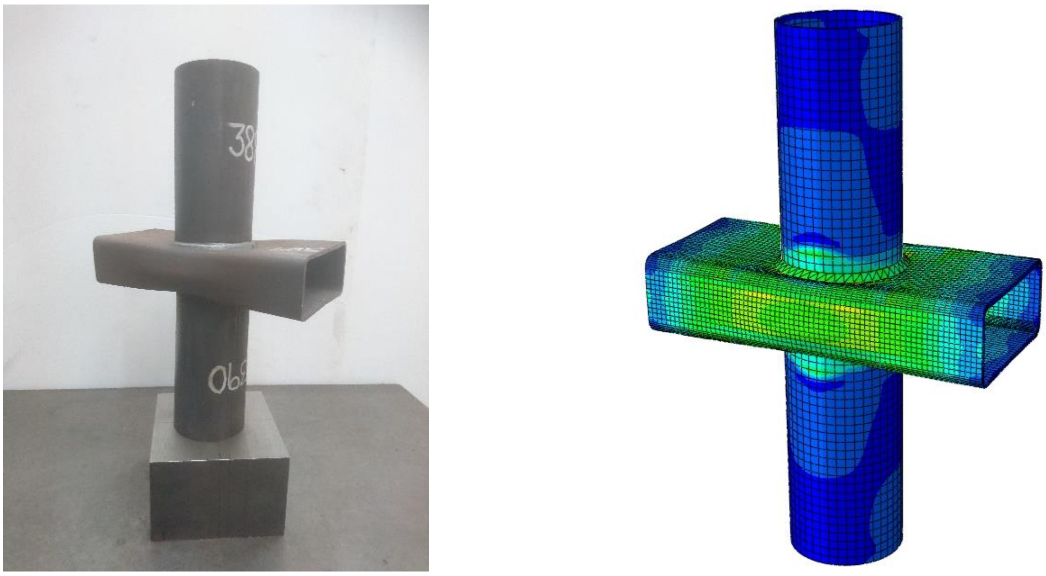

(a) Comparison of test and FE CHS-to-RHS X-joint failed by F mode.

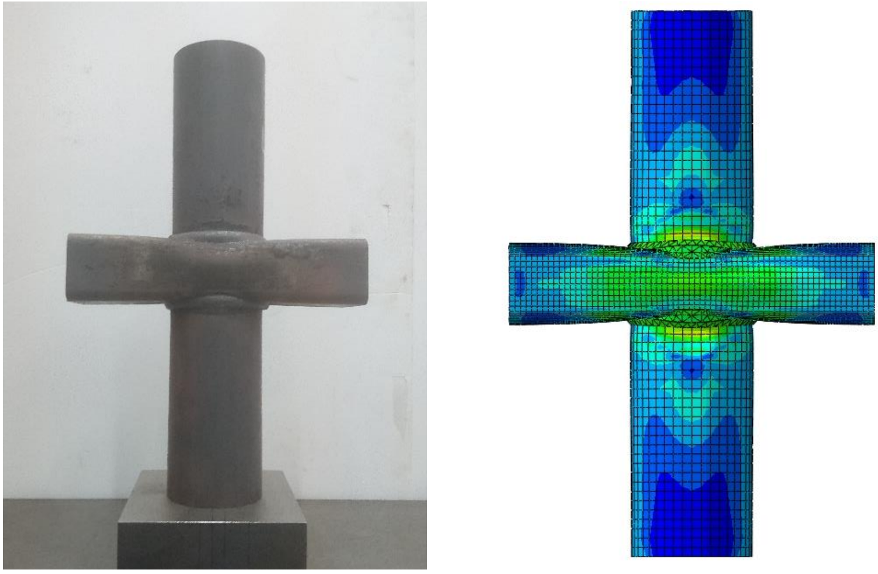

(b) Comparison of test and FE CHS-to-RHS X-joint failed by F+S mode.

Fig. 8. Failure modes comparisons between typical test and FE CHS-to-RHS X-joints.

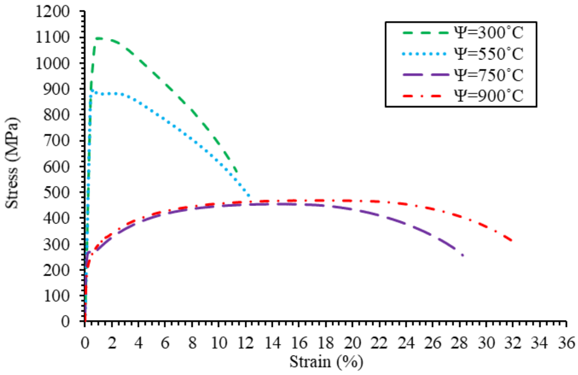

Fig. 9. Measured static post-fire stress-strain curves of CHS 88.9×4 [1].

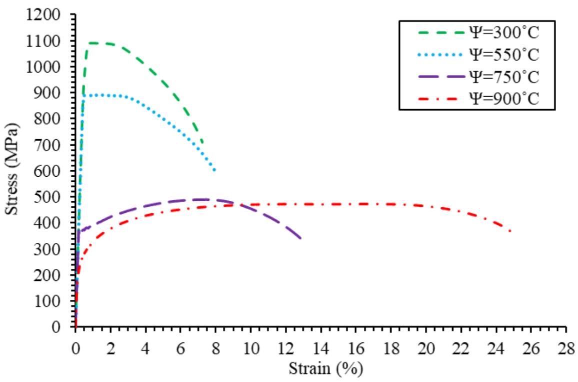

(a) Measured static post-fire stress-strain curves for flat portions of RHS 120×60×4.

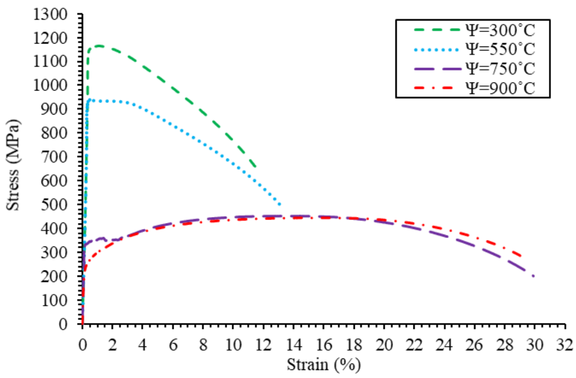

(b) Measured static post-fire stress-strain curves for corner portions of RHS 120×60×4.

Fig. 10. Measured static post-fire stress-strain curves of RHS 120×60×4 [1].

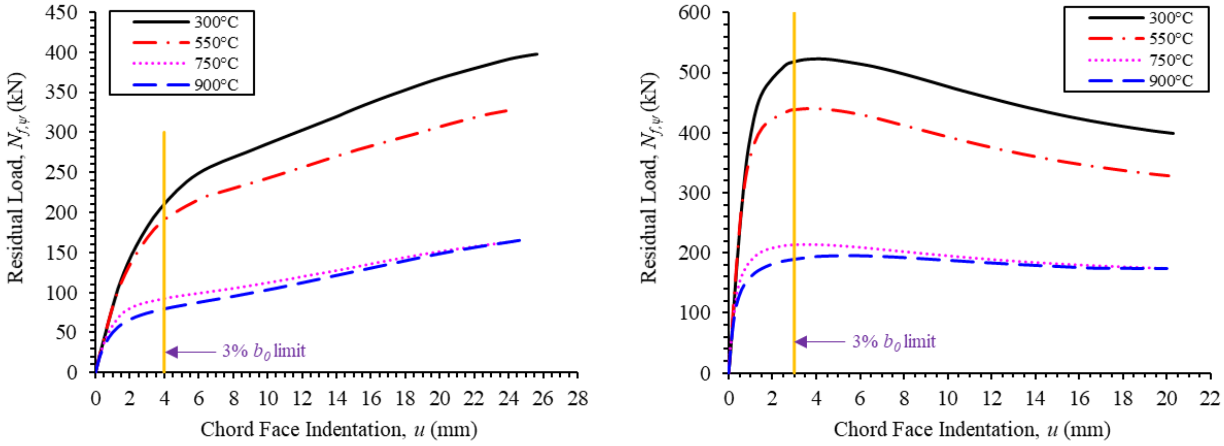

(a) For T-40×4-133×240×8 (β=0.30). (b) For T-80×6-100×100×6 (β=0.80).

Fig. 11. Variations of load-deformation curves for typical CHS-to-RHS T-joints failed by F and F+S modes for different fire exposures.

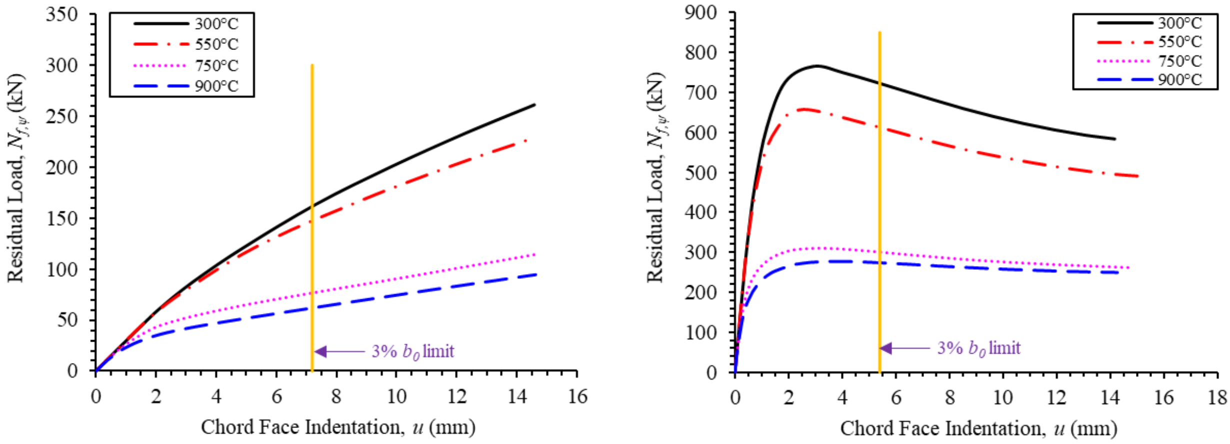

(a) For X-120×4.2-240×100×6 (β=0.50). (b) For X-162×6-180×100×6 (β=0.90).

Fig. 12. Variations of load-deformation curves for typical CHS-to-RHS X-joints failed by F and F+S modes for different fire exposures.

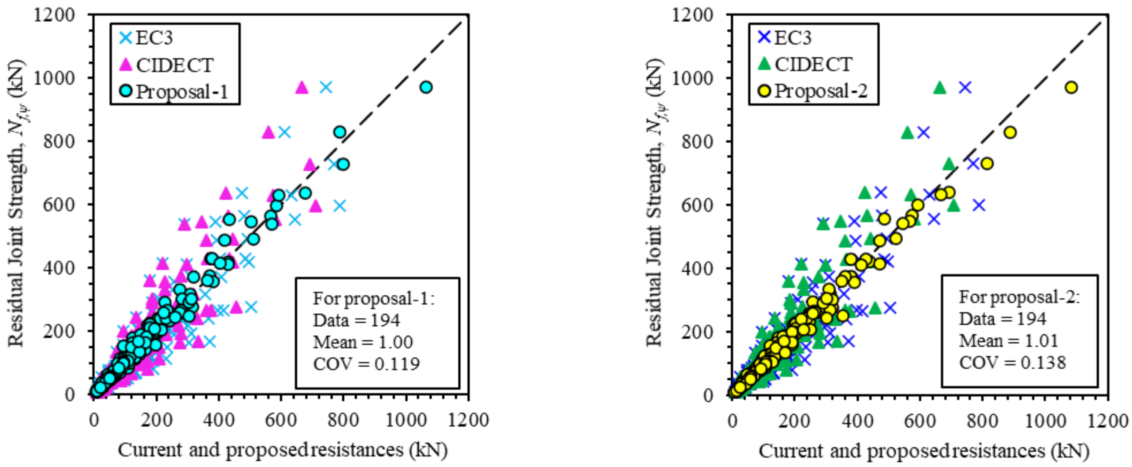

(a) For Proposal-1. (b) For Proposal-2.

Fig. 13. Comparisons of residual joint strengths with current and proposed nominal resistances for CHS-to-RHS T-joints failed by F mode.

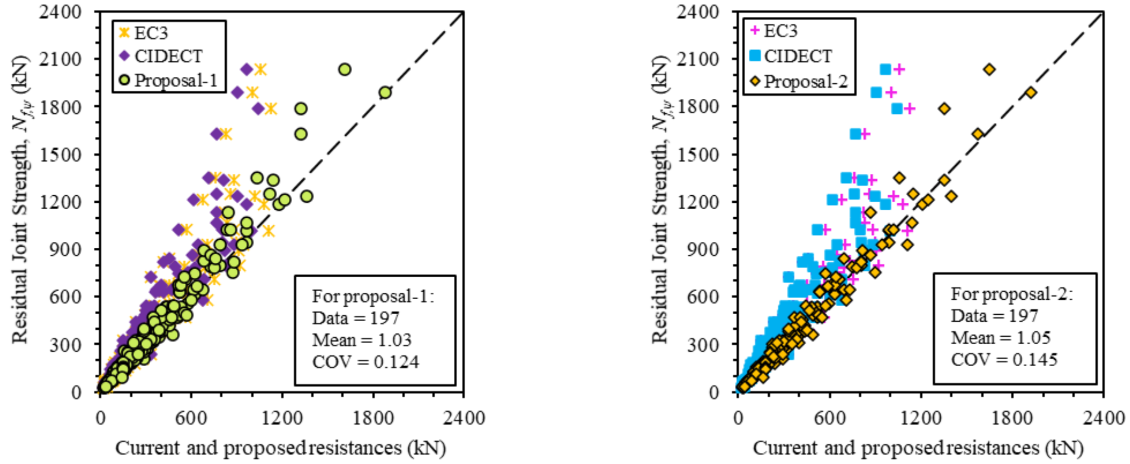

(a) For Proposal-1. (b) For Proposal-2.

Fig. 14. Comparisons of residual joint strengths with current and proposed nominal resistances for CHS-to-RHS T-joints failed by F+S mode.

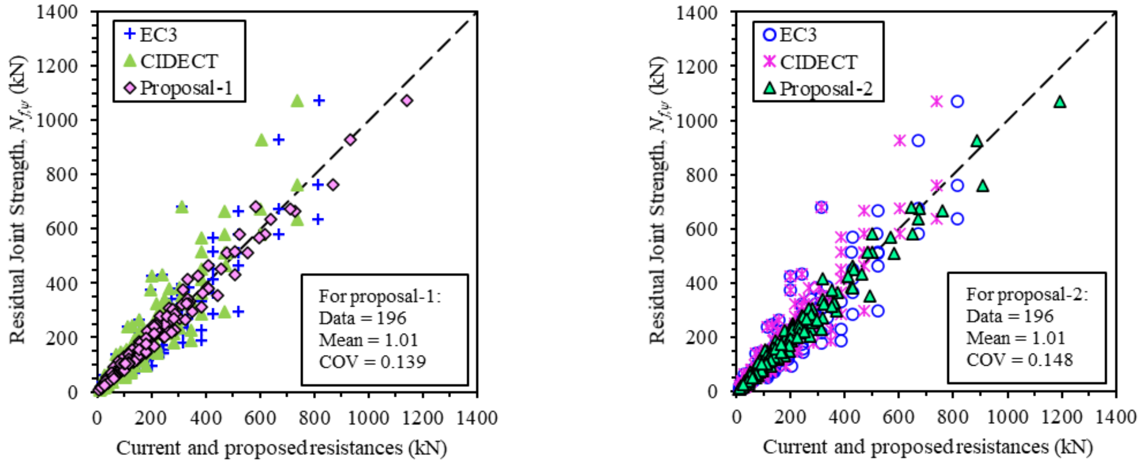

(a) For Proposal-1. (b) For Proposal-2.

Fig. 15. Comparisons of residual joint strengths with current and proposed nominal resistances for CHS-to-RHS X-joints failed by F mode.

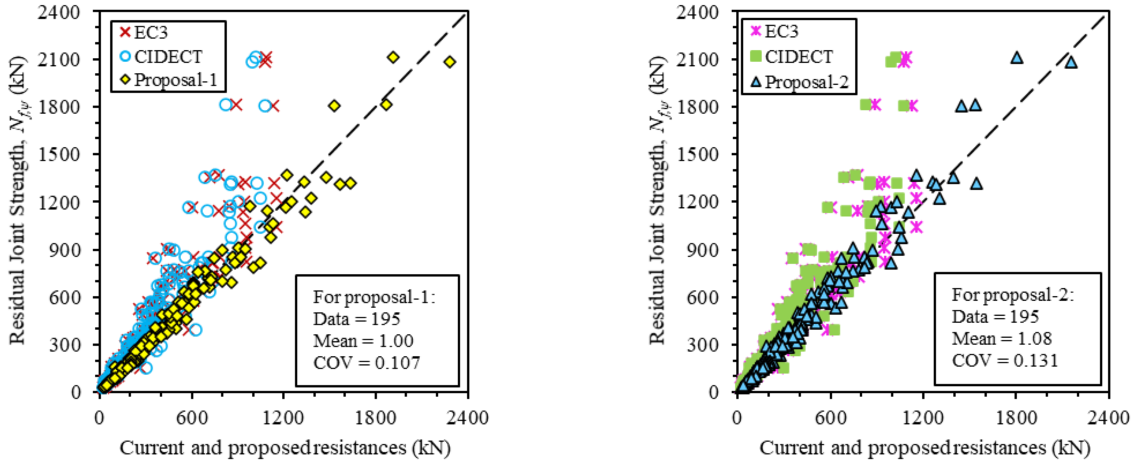

(a) For Proposal-1. (b) For Proposal-2.

Fig. 16. Comparisons of residual joint strengths with current and proposed nominal resistances for CHS-to-RHS X-joints failed by F+S mode.

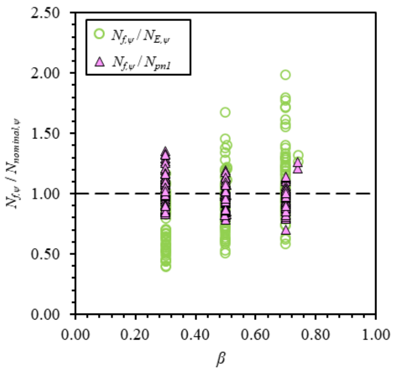

(a) EC3 [9] vs Proposal-1.

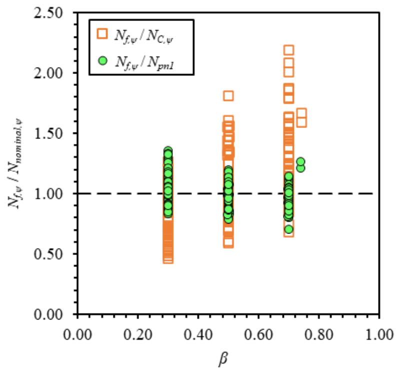

(b) CIDECT [10] vs Proposal-1.

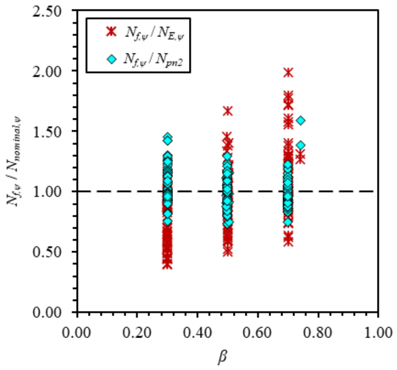

(c) EC3 [9] vs Proposal-2.

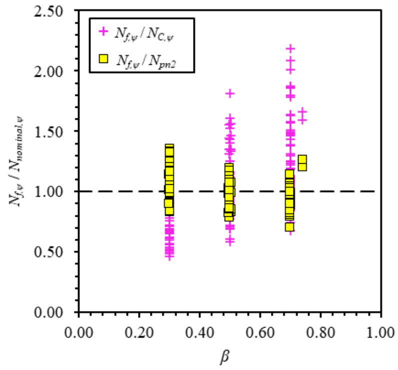

(d) CIDECT [10] vs Proposal-2.

Fig. 17. Distributions of residual joint strength-to-current and proposed nominal resistance comparison ratios for CHS-to-RHS T-joints failed by F mode.

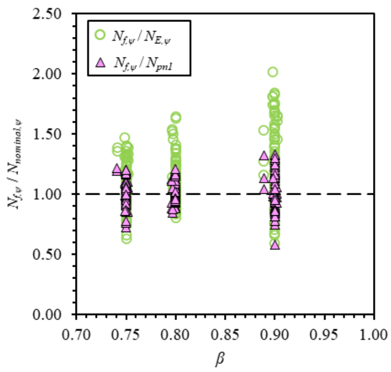

(a) EC3 [9] vs Proposal-1.

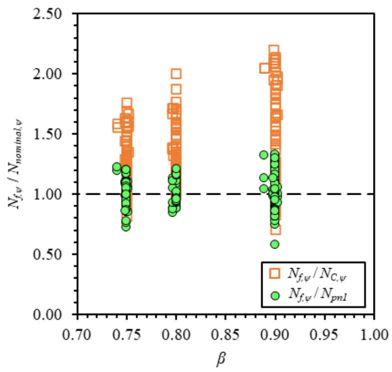

(b) CIDECT [10] vs Proposal-1.

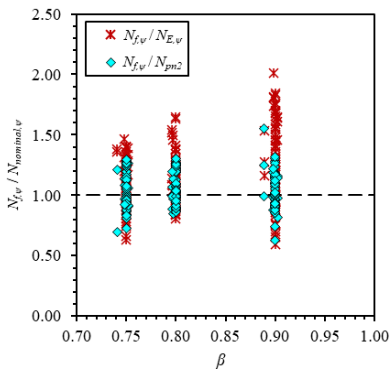

(c) EC3 [9] vs Proposal-2.

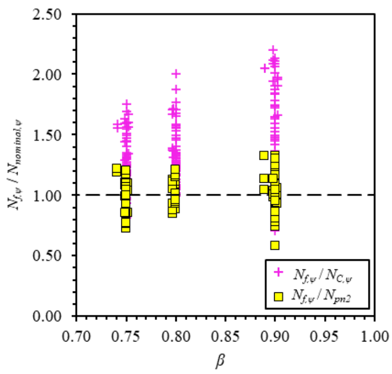

(d) CIDECT [10] vs Proposal-2.

Fig. 18. Distributions of residual joint strength-to-current and proposed nominal resistance comparison ratios for CHS-to-RHS T-joints failed by F+S mode.

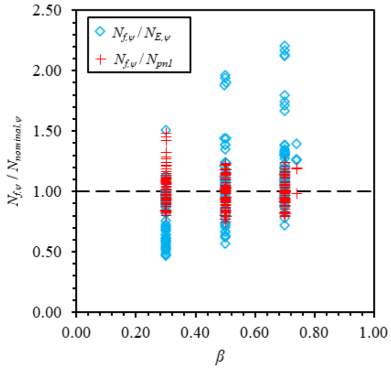

(a) EC3 [9] vs Proposal-1.

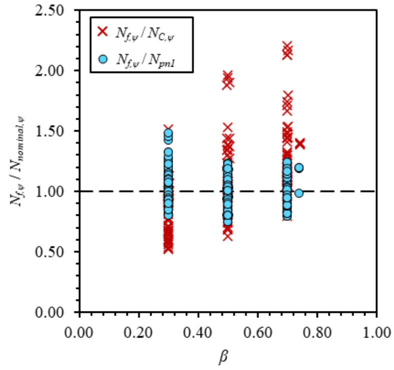

(b) CIDECT [10] vs Proposal-1.

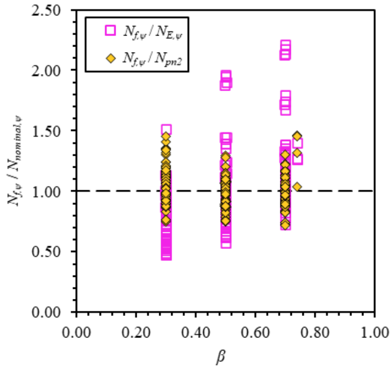

(c) EC3 [9] vs Proposal-2.

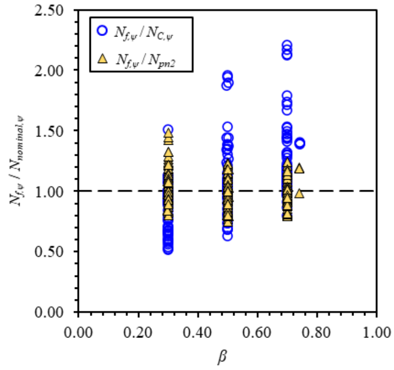

(d) CIDECT [10] vs Proposal-2.

Fig. 19. Distributions of residual joint strength-to-current and proposed nominal resistance comparison ratios for CHS-to-RHS X-joints failed by F mode.

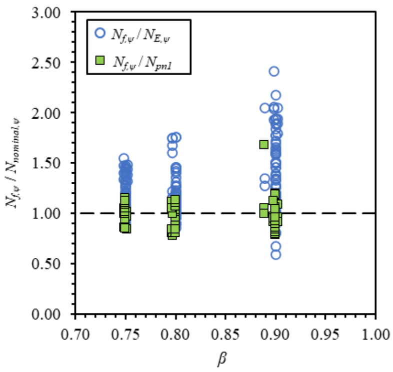

(a) EC3 [9] vs Proposal-1.

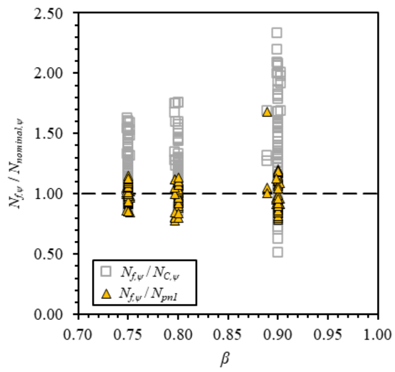

(b) CIDECT [10] vs Proposal-1.

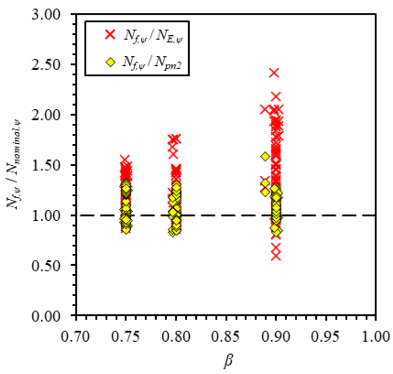

(c) EC3 [9] vs Proposal-2.

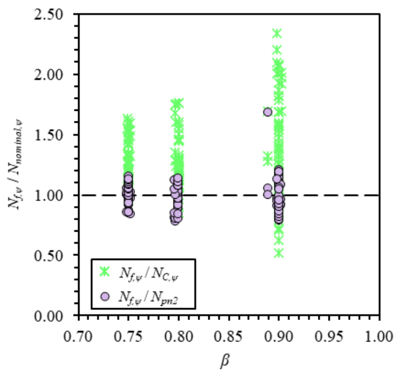

(d) CIDECT [10] vs Proposal-2.

Fig. 20. Distributions of residual joint strength-to-current and proposed nominal resistance comparison ratios for CHS-to-RHS X-joints failed by F+S mode.

Table 1. Test vs FE residual strength comparisons for CHS-to-RHS T-joints.

Specimen Numbers	Specimens T-d_1×t_1-b_0×h_0×t_0-Ψ	β	Test Strengths# (kN) $N_{f,\Psi}$	FE Strengths (kN) N_{FE}	$\frac{N_{f,\psi}}{N_{FE}}$
T1	T-88.9×4-100×60×4-P300˚C	0.89	292.2	288.7	1.01
T2	T-88.9×4-100×60×4-P550˚C	0.89	258.7	257.9	1.00
T3	T-88.9×3-120×60×4-P300˚C	0.74	178.5	174.1	1.03
T4	T-88.9×3-120×60×4-P550˚C	0.74	153.4	151.2	1.01
T5	T-88.9×4-100×60×4-P750˚C	0.89	112.0	110.3	1.02
T6	T-88.9×3-120×60×4-P750˚C	0.74	76.3	75.8	1.01
T7	T-88.9×3-120×60×4-P750˚C-R	0.74	78.1	75.9	1.03
				Mean (P_m)	1.02
				COV (V_p)	0.009

Note: #Data obtained from Pandey and Young [7].

Table 2. Test vs FE residual strength comparisons for CHS-to-RHS X-joints.

Specimen Numbers	Specimens X-d_1×t_1-b_0×h_0×t_0-Ψ	β	Test Strengths# (kN) $N_{f,\Psi}$	FE Strengths (kN) N_{FE}	$\frac{N_{f,\psi}}{N_{FE}}$
X1	X-88.9×4-100×60×4-P300°C	0.89	316.6	317.0	1.00
X2	X-88.9×4-100×60×4-P550°C	0.89	289.8	294.3	0.98
X3	X-88.9×3-120×60×4-P300°C	0.74	186.0	184.9	1.01
X4	X-88.9×3-120×60×4-P550°C	0.74	153.8	155.1	0.99
X5	X-88.9×4-100×60×4-P750°C	0.89	164.3	165.9	0.99
X6	X-88.9×3-120×60×4-P750°C	0.74	79.3	79.6	1.00
X7	X-88.9×3-120×60×4-P550°C-R	0.74	153.3	155.2	0.99
				Mean (P_m)	0.99
				COV (V_p)	0.007

Note: #Data obtained from Pandey and Young [7].

Table 3. Overall ranges of critical parameters used in parametric study.

Parameters	Validity Ranges
ψ	[300°C to 900°C]
β (d_1/b_0)	[0.30 to 0.90]
2γ (b_0/t_0)	[16.6 to 50]
h_0/t_0	[16.6 to 50]
τ (t_1/t_0)	[0.50 to 1.0]

Table 4. Post-fire material properties of tubular members used in parametric study [1].

Post-fire Temperatures (ψ)	Materials	Regions	Measured Post-fire Material Properties						
			E (GPa)	$\sigma_{0.2}$ (MPa)	$\varepsilon_{0.2}$ (%)	σ_u (MPa)	$0.80\sigma_u$ (MPa)	ε_u (%)	ε_f (%)
300°C	RHS (120×60×4)	Flat	214	1084	0.71	1090	872	1.00	7.23[a]
	RHS (120×60×4)	Corner	232	1161	0.70	1166	933	1.12	11.68[b]
	CHS (88.9×4)	Curved	207	1062	0.71	1096	877	1.04	11.32[b]
550°C	RHS (120×60×4)	Flat	219	889	0.61	891	713	1.37	8.10[a]
	RHS (120×60×4)	Corner	231	937	0.61	933	746	2.19	13.06[b]
	CHS (88.9×4)	Curved	214	893	0.62	882	706	2.17	12.45[b]
750°C	RHS (120×60×4)	Flat	207	371	0.38	491	392	7.44	13.17[a]
	RHS (120×60×4)	Corner	244	337	0.34	452	362	13.39	29.89[b]
	CHS (88.9×4)	Curved	198	269	0.34	455	364	14.32	28.23[b]
900°C	RHS (120×60×4)	Flat	200	257	0.33	473	378	16.56	25.01[a]
	RHS (120×60×4)	Corner	227	251	0.31	445	356	16.44	29.03[b]
	CHS (88.9×4)	Curved	202	233	0.32	469	375	17.30	32.39[b]

Note: [a]fracture strain based on 50 mm gauge length; [b]fracture strain based on 25 mm gauge length.

Table 5. Summary of comparisons between test and FE residual strengths with current and proposed nominal resistances for CHS-to-RHS T-joints failed by F mode.

Post-fire Temperatures (ψ)	Parameters	Comparisons			
		$\frac{N_{f,\psi}}{N_{E,\psi}}$	$\frac{N_{f,\psi}}{N_{C,\psi}}$	$\frac{N_{f,\psi}}{N_{pn1}}$	$\frac{N_{f,\psi}}{N_{pn2}}$
300°C	No. of data (n)	49	49	49	49
	Mean (P_m)	0.78	0.95	0.98	0.97
	COV (V_p)	0.294	0.315	0.081	0.096
550°C	No. of data (n)	49	49	49	49
	Mean (P_m)	0.81	0.98	1.02	1.10
	COV (V_p)	0.313	0.331	0.111	0.123
750°C	No. of data (n)	48	48	48	48
	Mean (P_m)	1.07	1.16	1.03	0.94
	COV (V_p)	0.290	0.308	0.114	0.114
900°C	No. of data (n)	48	48	48	48
	Mean (P_m)	1.10	1.20	0.97	1.04
	COV (V_p)	0.196	0.220	0.152	0.152
Overall	No. of data (n)	194	194	194	194
	Mean (P_m)	0.94	1.07	1.00	1.01
	COV (V_p)	0.309	0.307	0.119	0.138
	Resistance factor (ϕ)	1.00	1.00	0.80	0.80
	Reliability index (β_0)	1.03	1.46	2.63	2.59

Table 6. Summary of comparisons between test and FE residual strengths with current and proposed nominal resistances for CHS-to-RHS T-joints failed by F+S mode.

Post-fire Temperatures (*ψ*)	Parameters	Comparisons $\frac{N_{f,\psi}}{N_{E,\psi}}$	$\frac{N_{f,\psi}}{N_{C,\psi}}$	$\frac{N_{f,\psi}}{N_{pn1}}$	$\frac{N_{f,\psi}}{N_{pn2}}$
300°C	No. of data (n)	49	49	49	49
	Mean (P_m)	1.13	1.41	1.02	1.02
	COV (V_p)	0.272	0.251	0.129	0.132
550°C	No. of data (n)	49	49	49	49
	Mean (P_m)	1.08	1.34	0.99	1.14
	COV (V_p)	0.226	0.238	0.092	0.105
750°C	No. of data (n)	51	50	51	51
	Mean (P_m)	1.25	1.39	1.09	0.94
	COV (V_p)	0.180	0.197	0.097	0.106
900°C	No. of data (n)	48	48	48	48
	Mean (P_m)	1.21	1.36	1.02	1.10
	COV (V_p)	0.233	0.243	0.154	0.154
Overall	No. of data (n)	197	197	197	197
	Mean (P_m)	1.17	1.37	1.03	1.05
	COV (V_p)	0.233	0.231	0.124	0.145
	Resistance factor (ϕ)	1.00	1.00	0.85	0.80
	Reliability index (β_0)	1.83	2.42	2.50	2.69

Table 7. Summary of comparisons between test and FE residual strengths with current and proposed nominal resistances for CHS-to-RHS X-joints failed by F mode.

Post-fire Temperatures (*ψ*)	Parameters	Comparisons $\frac{N_{f,\psi}}{N_{E,\psi}}$	$\frac{N_{f,\psi}}{N_{C,\psi}}$	$\frac{N_{f,\psi}}{N_{pn1}}$	$\frac{N_{f,\psi}}{N_{pn2}}$
300°C	No. of data (n)	49	49	49	49
	Mean (P_m)	0.87	0.96	1.03	0.97
	COV (V_p)	0.279	0.279	0.117	0.126
550°C	No. of data (n)	50	50	50	50
	Mean (P_m)	0.91	1.01	1.07	1.12
	COV (V_p)	0.272	0.272	0.089	0.106
750°C	No. of data (n)	49	49	49	49
	Mean (P_m)	1.20	1.20	1.10	0.95
	COV (V_p)	0.332	0.332	0.163	0.163
900°C	No. of data (n)	48	48	48	48
	Mean (P_m)	1.16	1.16	0.99	1.01
	COV (V_p)	0.197	0.197	0.144	0.144

Overall	No. of data (n)	196	196	196	196
	Mean (P_m)	1.03	1.08	1.01	1.01
	COV (V_p)	0.310	0.289	0.139	0.148
	Resistance factor (ϕ)	1.00	1.00	0.80	0.80
	Reliability index (β_0)	1.27	1.54	2.58	2.55

Table 8. Summary of comparisons between test and FE residual strengths with current and proposed nominal resistances for CHS-to-RHS X-joints failed by F+S mode.

Post-fire Temperatures (ψ)	Parameters	Comparisons $\frac{N_{f,\psi}}{N_{E,\psi}}$	$\frac{N_{f,\psi}}{N_{C,\psi}}$	$\frac{N_{f,\psi}}{N_{pn1}}$	$\frac{N_{f,\psi}}{N_{pn2}}$
300°C	No. of data (n)	49	49	49	49
	Mean (P_m)	1.26	1.35	0.99	1.05
	COV (V_p)	0.253	0.239	0.097	0.099
550°C	No. of data (n)	49	49	49	49
	Mean (P_m)	1.20	1.29	0.96	1.18
	COV (V_p)	0.224	0.227	0.085	0.098
750°C	No. of data (n)	49	49	49	49
	Mean (P_m)	1.34	1.30	1.04	0.94
	COV (V_p)	0.223	0.212	0.120	0.098
900°C	No. of data (n)	48	48	48	48
	Mean (P_m)	1.33	1.30	1.01	1.14
	COV (V_p)	0.259	0.265	0.110	0.110
Overall	No. of data (n)	195	195	195	195
	Mean (P_m)	1.28	1.31	1.00	1.08
	COV (V_p)	0.243	0.235	0.107	0.131
	Resistance factor (ϕ)	1.00	1.00	0.80	0.85
	Reliability index (β_0)	2.06	2.26	2.68	2.63